

Article

Determining the Relation between Groundwater Flow Velocities and Measured Temperature Differences Using Active Heating-Distributed Temperature Sensing

Wiecher Bakx ^{1,2,*} , Pieter J. Doornenbal ³, Rebecca J. van Weesep ⁴, Victor F. Bense ⁵, Gualbert H. P. Oude Essink ^{3,6}  and Marc F. P. Bierkens ⁶

¹ Wetsus, European Centre of Excellence for Sustainable Water Technology, Oostergoweg 9, 8911 MA Leeuwarden, The Netherlands

² Department of Watermanagement, Arcadis Nederland B.V., Beaulieustraat 22, 6814 DV Arnhem, The Netherlands

³ Department of Subsurface and Groundwater, Deltares, P.O. Box 85467, 3508 AI Utrecht, The Netherlands

⁴ Nelen & Schuurmans, Zakkendragershof 34, 3511 AE Utrecht, The Netherlands

⁵ Hydrology and Quantitative Water Management, Department of Environmental Sciences, Wageningen University, P.O. Box 47, 6700 AA Wageningen, The Netherlands

⁶ Department of Physical Geography, Utrecht University, 3584 CS Utrecht, The Netherlands

* Correspondence: wiecher.bakx@arcadis.com

Received: 12 July 2019; Accepted: 1 August 2019; Published: 5 August 2019



Abstract: Active Heating-Distributed Temperature Sensing (AH-DTS) has the potential to allow for the measurement of groundwater flow velocities in situ. We placed DTS fiber-optic cables combined with a heating wire in direct contact with aquifer sediments in a laboratory scale groundwater flow simulator. Using this setup, we empirically determined the relationship between ΔT , the temperature difference by constant and uniform heating of the DTS cable and the background temperature of the groundwater system, and horizontal groundwater flow velocity. Second, we simulated the observed temperature response of the system using a plan-view heat transfer flow model to calibrate for the thermal properties of the sediment and to optimize cable setup for sensitivity to variation in groundwater flow velocities. Additionally, we derived an analytical solution based on the heat flow equation that can be used to explicitly calculate flow velocity from measured ΔT for this specific AH-DTS cable setup. We expect that this equation, after calibration for cable constitution, is valid for estimating groundwater flow velocity based on absolute temperature differences measured in field applications using this cable setup.

Keywords: distributed temperature sensing; groundwater monitoring; groundwater velocities

1. Introduction

Continuous monitoring of groundwater flow velocities provides insights into, e.g., groundwater recharge, movement of solutes (contaminants as well as salts), the rates of interaction between groundwater and surface water, and interference between Aquifer Thermal Energy Systems [1,2]. However, quantitative groundwater flow measurements can be challenging [3] and various methods for the monitoring of groundwater flow are available that all have their strengths and weaknesses. Hydraulic head observations in piezometers or boreholes, allow for mapping hydraulic gradients in aquifers and can be used to estimate regional flow patterns indirectly. However, to estimate groundwater flow, such measurements will be uncertain due to the largely unknown heterogeneity

and anisotropy of hydraulic conductivities in most aquifers. Groundwater flow velocity can directly be estimated via the use of geochemical tracers, either natural or introduced anthropogenically. But for accurate tracing, tracers need to be tracked over a significant distance (e.g., 100 s of meters) and, given low groundwater flow velocities, this would generally involve long-lasting field experiments. Geophysical characterization techniques, such as direct current resistivity, self-potential and induced polarization are available, with the advantage that they cover large subsurface volumes, enabling the elucidation of hydrogeological structures and infer preferential flow pathways. However, they usually do not yield a quantitative measure of groundwater flow velocity, while single well point dilution methods have also proven to be reliable methods for estimating groundwater flow [4,5]. Recently, successful attempts were reported considering the direct measurement of groundwater flow velocities using heat as a tracer in open boreholes [6], using fiber-optic cables in direct contact with the aquifer [7] and in dams/dykes [6–8]. Distributed Temperature Sensing (DTS) along fiber-optic cables has played an important role in these developments [9]. One DTS method, namely Active Heating-Distributed Temperature Sensing (AH-DTS), employs a fiber-optic cable to measure temperature in combination with a heating source, usually a separate heating element, or injected water with an anomalous temperature. The relation between the transient temperature response and groundwater flow will depend on the thermal inertia of the passive cable used to detect this response, the thermal properties of the lithology and the rate and direction of groundwater flow close to the cable [6,8,9]. Several studies applied the AH-DTS setup in boreholes and well screens to estimate the inflow of groundwater and the background groundwater flow itself, where DTS cables are placed in the bore of uncased boreholes, mostly in fractured rock settings [6,10–13]. The potential of the AH-DTS methodology using cables in direct contact with unconsolidated sediments was first shown by [7]. They introduced a separate heating element upstream of DTS cables that were installed in the aquifer by direct-push methods. Recently an analytical solution was provided to estimate specific discharge using an AH-DTS setup by solving four constants [14]. Advantage of this solution is that the relative position of the heat source to the temperature measurement location is not needed.

In this study, we interpret data from a laboratory experiment to assess the relationship between groundwater flow velocity and the temperature difference measured in an Active Heating-Distributed Temperature Sensing (AH-DTS) setup. Making use of a groundwater flow simulator in a laboratory setting, a fiber-optic cable with a heating wire attached to the cable was placed in direct contact with unconsolidated sandy sediments. By applying electrical power to the heating cable, the AH-DTS cable was actively heated, creating a constant heat input for a fixed period of time. By measuring the temperature change at the same time, the maximum temperature difference (ΔT) with respect to the pre-heating period was obtained, which was assumed to relate to groundwater flow velocity. To empirically estimate the ΔT -velocity relationship, ΔT was determined for different groundwater flow velocities. A numerical heat transport model was used to estimate the thermal properties of the sediment, and analyzed and optimized the cable setup. An analytical solution to the heat flow equation was fitted to the measured data, which can be used in field applications with the advantage that only two parameters need to be estimated, specific to the cable setup used.

2. Materials and Methods

Two cycles of laboratory experiments were carried out at the laboratory of the Deltares research facility in Delft, the Netherlands. The groundwater flow simulator used there is described below (Section 2.1). The first set of experiments took place between 29 May–3 August 2017 and the second set of experiments between 23 July–23 August 2018. The setup of the AH-DTS system is described in Section 2.2. Results of the experiments and their interpretation using both a numerical and analytical model are described in Sections 2.3 and 2.4.

2.1. Laboratory Setup Flow Simulator

The flow simulator used is visualized in Figure 1. The system is based on a 2 m long, 1 m wide and 1 m high tank containing the sediment and measurement equipment. Water enters and leaves the tank through the short sides of the tank using six perforated tubes on each side with vertical slots of 0.5 mm covering the complete width and height of the tank to ensure an evenly distributed in-and outflow. The inflow of the system is connected with hoses to a separate water tank of approximately $60 \times 10^{-3} \text{ m}^3$ (when filled) and kept at a constant water level using a pump and spillway. By changing the height of the inflow water tank and the height of the outflow hose on the downstream side of the tank, the hydraulic head difference between in- and outflow of the tank was controlled and so was the groundwater velocity within the simulator. Groundwater flow velocities (Darcy flux) between 0.1 and 8 m d^{-1} were generated in this way. The background temperature inside the flow simulator was not constant during the experiments, due to shutting down the flow overnight (in the 2017 experiments) and changing inflow temperatures, despite the fact that the temperature of the hall, in which the simulator was placed, was kept constant at $20 \text{ }^\circ\text{C}$. During the 2018 experiments, flow was continued overnight for a more stable background temperature.

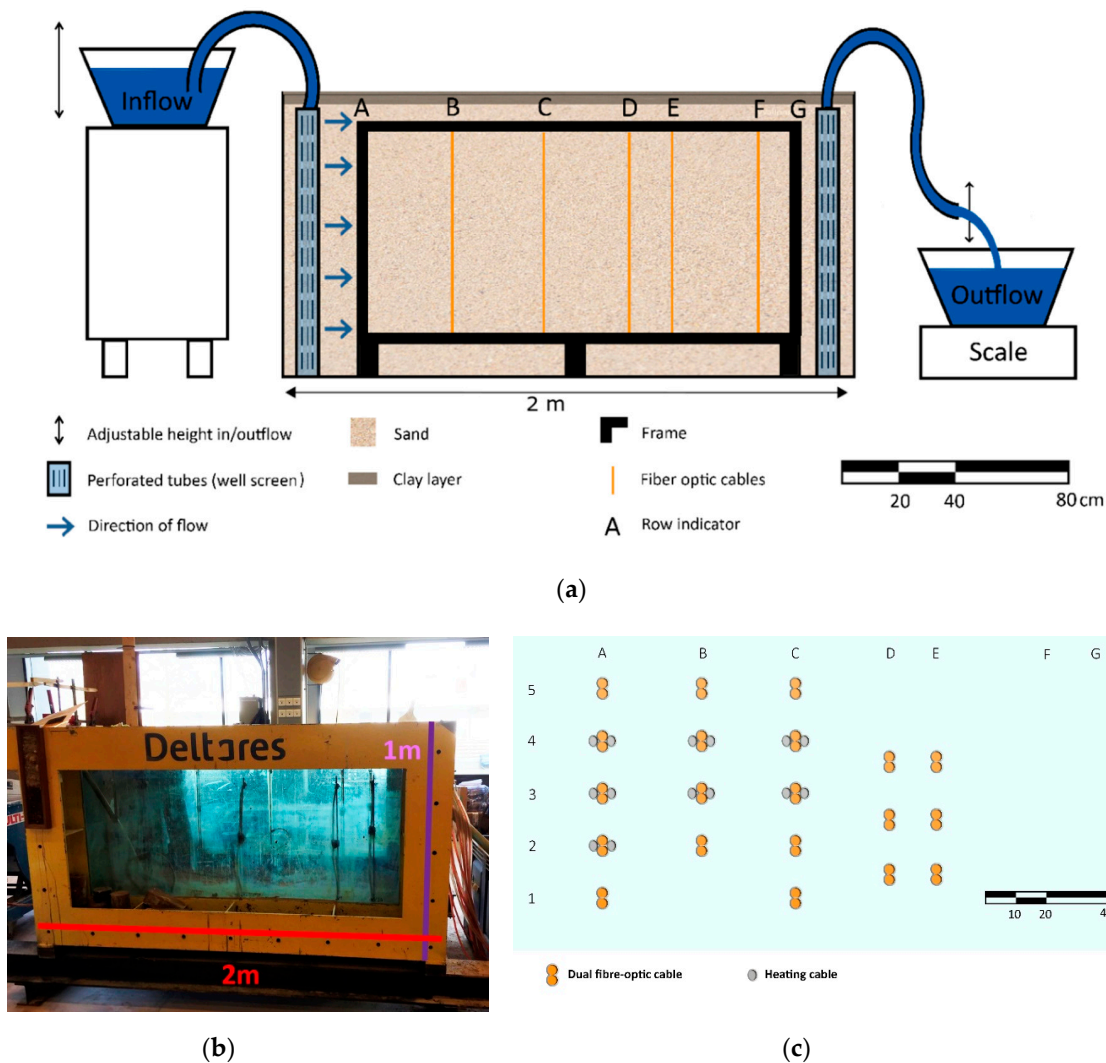


Figure 1. (a) Schematic side view of the flow simulator, in 2D vertical view. The frame contains the Distributed Temperature Sensing (DTS) cables and is placed inside the tank [15]; (b) Sideview picture of the flow simulator showing the dimensions; (c) schematic top view of the cable locations as placed in the flow simulator. The cable locations selected for the FlexPDE modeling are A3 and A4 (see Section 2.3).

A frame placed inside the flow simulator (diameter of frame tubes 5 cm, Figure 1b) was used to hold the AH-DTS cables and the tank was filled with water followed by the sediment. The tank was filled manually with sand to ensure an even distribution without density and settling difference covering the frame for about 5 cm. The sand was sealed by placing a clay layer of ca. 4 cm thick on the top of the sediment, so as to prevent water from flowing over the sediment. A weight was placed on top of the clay layer for additional pressure. Both the uniform placement of the sand and the in-and-outflow system ensured as even and constant a flow as possible within the simulator. For the 2018 experiments, sand with a diameter of 0.8–1.25 mm was used. The porosity (0.41) and the hydraulic conductivity (40 m d^{-1}) of the sediment were experimentally determined after the flow and heat transport experiment.

Flow in the flow simulator was monitored by weighing the outflow over time resulting in the discharge rate of the simulator and by measuring hydraulic head differences at 24 locations within the flow simulator placed at ca. 12.5 cm and 75 cm above the bottom of the simulator and 5 cm from each sidewall of the simulator. Four locations were located in the center of the tank attached to the frame. After changing the flow velocities in the setup, sufficient time was given to establish a hydraulic steady-state. The hydraulic head measurements were used to confirm a hydraulic steady-state.

2.2. Measuring Temperature Using AH-DTS

The temperature in the flow simulator was recorded continuously using the AH-DTS setup and PT100 sensors. DTS measurements were done using the Silixa Ultima DTS instrument (Silixa, London, UK) measuring temperature for 1 s per channel with a spatial sampling interval of 0.125 m. For every vertically placed AH-DTS cable segment the collected samples over the length of the cable segment (90 cm) were averaged to a single temperature result.

A section at the beginning and end of the fiber-optic cable was run through a relatively warmer and cooler reference bath to calibrate the data resulting in a mean absolute error of $0.21 \text{ }^{\circ}\text{C}$ (Figure 2a,b) using a single ended calibration method following [16]. Reference temperature data was collected using PT100 sensors. Data from the PT100 sensors were acquired by Ecograph RSG30 (Edress + Hauser, Reinach, Switzerland). During the 2017 experiments different types of fiber-optic cables including heating elements were tested and modeled. This included cable setups with a heating element within the mantle of the fiber-optic cable or separate from the fiber-optic cable. The latest also with variation in thickness of the fiber-optic cable protective elements (PVC and aramid protection). The cable setup with a separate heating wire outside of the fiber-optic cable and relatively thin protective elements resulted in the highest ΔT groundwater flow velocity relation. Based on the results of this cable setup and modeling, an optimal active heating cable setup was constructed for the 2018 experiments. The fiber-optic cable used in the 2018 experiment is a multimode duplex cable produced by LEONI [17], also used in the 2017 experiment. The 2017 cable setup contained a duplex fiber-optic cable using an additional jacket holding the two fiber-optic cables together (Figure 3a). A single separate heating wire was used. The 2018 duplex fiber-optic cable did not have a jacket and the two heating wires were glued directly to the fiber-optic cables (Figure 3b). Heat in the heating wires was created by applying an electrical current to the wire and the resistance of the cable causing an even heating of the wire. The 2017 experiments proved useful for optimizing the cable and experimental setup for the 2018 experiments. The 2018 experiments provided a better dataset and therefore, we restricted the modeling and results presented in this article to the 2018 experiments.

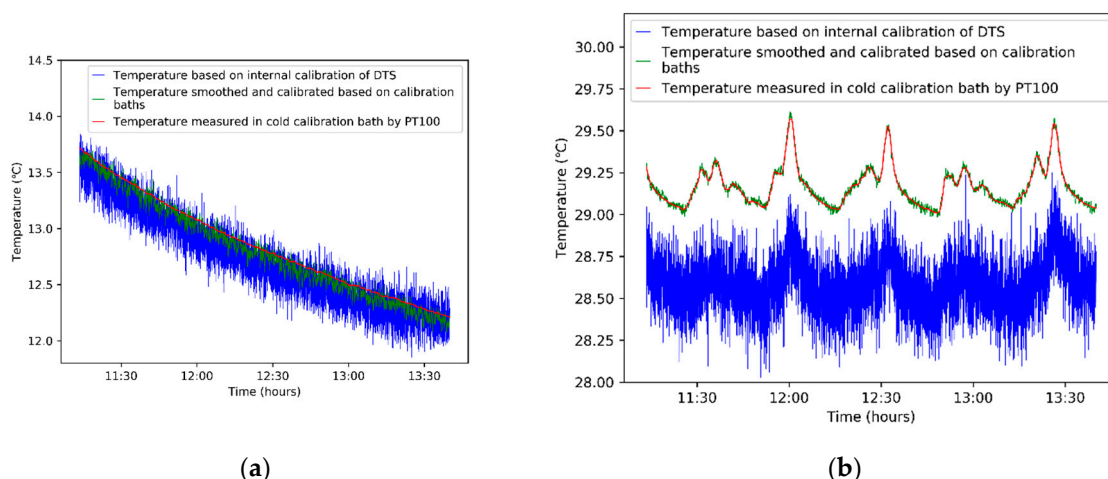


Figure 2. (a) Temperatures for the cable section placed in the cooler reference temperature bath based on internal calibration of the Silixa Ultima DTS (blue), Calibrated and smoothed temperature based on the separated calibration bath (green) and PT100 measurement data of the temperature in the calibration bath (red); (b) Temperatures for the cable section placed in the warmer reference temperature bath.

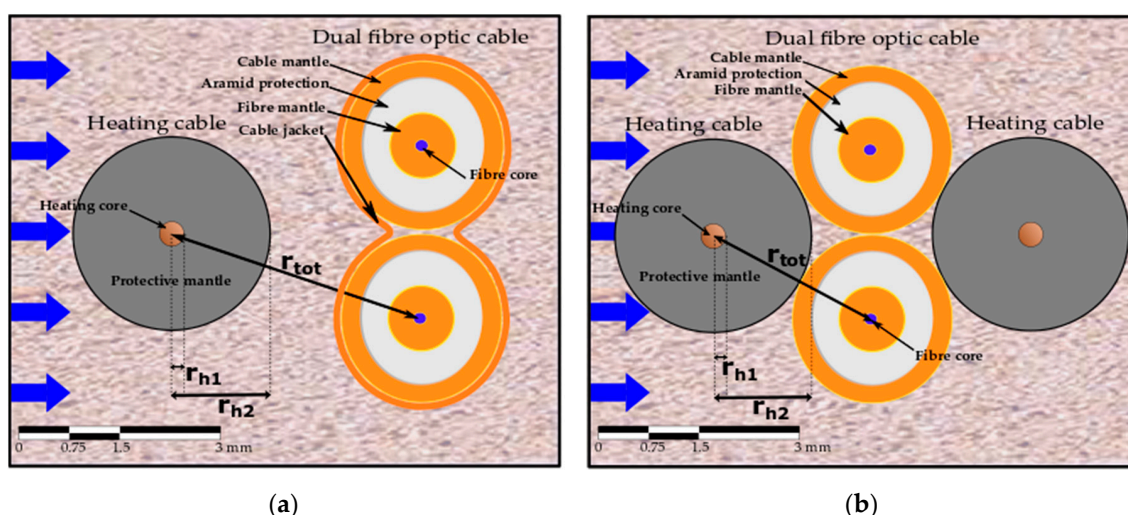


Figure 3. Cross-section showing the setup of the heating cable and the fiber-optic cables. (a) Cable setup for the 2017 experiments; (b) Improved cable setup for the 2018 experiments.

In all experiments the groundwater flow velocity was regulated and kept constant at a known value. The AH-DTS setup was continuously measuring, with a temporal interval of 1 s. Heat was introduced by applying electrical power to the heating cables, resulting in an evenly distributed heat along the cable due to cable resistance. In an experimental run, heat was applied for a period of 90–120 min until the measured temperature by the DTS started to level out. For every groundwater flow velocity, each experiment was repeated at least once.

The measurement temperature of the DTS for the experimental runs clearly shows the resulting temperature difference (ΔT) due to heating. Two issues that needed to be addressed to improve the determination of ΔT were (1) the fact that the equilibrium during heating was not completely reached, and (2) the drift in the background temperature. A function was fitted through the heating curve (using MATLAB[®] Curve Fitting Toolbox) to determine the equilibrium temperature as being the asymptote of the heating curve using:

$$\Delta T = \frac{a}{bt + c} + d \tag{1}$$

where d is the asymptote of the equilibrium temperature (a is related to the start value at $t = 0$, b determines the curvature of the solution and c the location of the change in exponential relation) and an average R^2 of 0.80 over all heating curve fits. To correct for the drift in the background temperature the base temperature after each heating run was determined by fitting an exponential function on the cooling curve using:

$$\Delta T = a^{-bt} + e \quad (2)$$

which is consistent with Newton's Law of Cooling. The base temperature for ΔT was taken from e being the asymptote of this curve (a related to the start value at $t = 0$ and b the curvature of the solution) and the average R^2 of all cooling curve fits was 0.79. The resulting base temperature (based on the asymptote e) was subtracted from the asymptote of the equilibrium temperature resulting in a more consistent ΔT . We chose this method because shortening the heating periods can be a great advantage for field applications.

2.3. Numerical Modeling

To estimate the thermal properties of the sediment-fluid matrix and to optimize the cable setup, we constructed a numerical model of the experimental flow simulator including the AH-DTS cables using the software FlexPDE (PDE Solutions, Inc., Spokane Valley, WA, USA). Both a differential equation for groundwater flow and heat transfer were solved. The model contains a 2D schematization of a horizontal cross-section of the laboratory setup (2 m \times 1 m). Vertical variations were not included, assuming no vertical differences in temperature or flow, and flow being only directed perpendicular to the cables. The differential equation solving the steady-state groundwater flow is given by (assuming a homogeneous medium with horizontal isotropy):

$$k_h \left(\frac{\partial^2 h}{\partial x^2} + \frac{\partial^2 h}{\partial y^2} \right) = 0 \quad (3)$$

where k_h is the hydraulic conductivity (m s^{-1}), h is the hydraulic head (m) and x and y are the distance (m). The heat transfer is represented by the heat transport equation [18]:

$$\rho_b c_b \frac{\partial T}{\partial t} = k_{eff} \left(\frac{\partial^2 T}{\partial x^2} + \frac{\partial^2 T}{\partial y^2} \right) - \rho_w c_w \left(q_x \frac{\partial T}{\partial x} + q_y \frac{\partial T}{\partial y} \right) + \frac{Q}{A} \quad (4)$$

where ρ_b/ρ_w and c_b/c_w respectively are the bulk density (kg m^{-3}) and the bulk specific heat capacity ($\text{J kg}^{-1} \text{ }^\circ\text{C}^{-1}$) of the saturated sediment (b) and that of water (w), T is the temperature ($^\circ\text{C}$), t is time (seconds) and k_{eff} is the effective thermal conductivity of water and solids, ($\text{W m}^{-1} \text{ }^\circ\text{C}^{-1}$). q_x and q_y are the components of the specific discharge vector:

$$q_{x,y} = -k_{x,y} \frac{\partial h}{\partial x,y} \quad (5)$$

which results from solving Equation (3). Heat is introduced in the term $\frac{Q}{A}$, where Q (W m^{-1}) is the input of heat to the heating cable and A (m^2) is the cross-sectional area of the heating wire. The parameters used for the heat input and the sediment properties are given in Table 1.

The temperature of inflowing water measured by a PT100 sensor was used as a boundary condition for the temperature on the left side border of the flow simulator resulting in background temperatures in the model corresponding to the laboratory experiments. For the right-side border, the outflowing heat flux was defined as the advective component of heat flow (second term on the righthand side in Equation (4)). The top and bottom boundaries of the model were defined as zero flow and zero heat outflow flux. Two specific cable locations within the sediment of the flow simulator were included in the model, location A3 ($x = 0.229$ m, $y = 0.5145$ m) and location A4 ($x = 0.229$ m, $y = 0.646$ m). Material

properties of the cable components were derived from manufacturer specifications or the literature, or used as a calibration parameter and presented in Table 2.

Table 1. Specific properties and parameters as used in the FlexPDE model.

Parameter	Parameter	Reference
Heat input Q (W m ⁻¹)	33.33	Based on measured voltage input and cable resistance
Horizontal hydraulic conductivity (m d ⁻¹)	40	Determined in laboratorial experiments
Effective porosity (-)	0.41	Determined in laboratorial experiments

Location A4 (Figure 1b) was used for calibration of the model. Location A3 (Figure 1b) was used as validation location. Measurements from the laboratory experiments of 30 July 2018 were used as input values for velocity, inflow temperature and the start- and stop-time of power input to the DTS cables in the model. Two experimental runs with different groundwater flow velocities were used (0.94 m d⁻¹, 1.89 m d⁻¹).

Table 2. Specific properties of cable components as used in the FlexPDE model.

Medium	Thermal Conductivity (W m ⁻¹ K ⁻¹)	Specific Heat (J kg ⁻¹ K ⁻¹)	Density (g cm ⁻³)	Reference
Sand	5.1 ¹	830	2.65	[19–21]
Water	0.591	4186	0.99	[19]
Heating cable core	390	385	8.96	
Heating cable protection material	0.2	100	1.2	[22]
DTS protective jacket	0.196	1565	1.121	[23]
DTS aramid protection	0.04	1420	1.44	[24]
DTS fiber mantle	0.196	1565	1.121	[23]
DTS fiber	2	1430	2.2	[25]

¹ The thermal conductivity of sand was used as the calibration parameter of the model.

2.4. Analytical Solution for Direct Groundwater Flow Velocity Estimation Using ΔT

The disadvantage of using an empirical relationship between ΔT and groundwater flow velocity is that it may be difficult to use in geological materials that are very different from those used in our experiments. Therefore, a more physically based approach is more suitable for our purposes.

Read et al. [6] applied an equation to describe the temperature change (ΔT in °C) by combining the heat transfer due to convection based on Newton's Law of Cooling with the heat transfer due to conduction based on Fourier's Law suitable for a fiber-optic cable heated from within. In our setup (Figure 3b), the heated element was outside of the fiber-optic cable, resulting in a modified version to include the heat transfer through the sediment of the equation by [6]:

$$\Delta T = \frac{Q}{2\pi} \left(\frac{1}{h r_{h2}} + \frac{1}{k_{tot}} \ln \frac{r_{tot}}{r_{h1}} \right) \quad (6)$$

where Q is the heat input to the cable (W m⁻¹), r_{h1} (m) is the radius of the heating part of the heating cable (m), r_{h2} (m) is the total radius of the heating cable and r_{tot} (m) is the sum of the radii of the heating cable, the distance through the sediment and the radius of the fiber-optic cable used to measure temperature change combined. k_{tot} (W m⁻¹ K⁻¹) is the combined thermal conductivity calculated (harmonic mean) as materials in series [26]:

$$k_{tot} = \frac{1}{\frac{f_{hc}}{k_{hc}} + \frac{f_h}{k_h} + \frac{f_j}{k_j} + \frac{f_a}{k_a} + \frac{f_m}{k_m} + \frac{f_f}{k_f} + \frac{f_{sed}}{k_{eff}}} \quad (7)$$

where the thermal conductivity (see Table 2) and the fraction of the thickness in respect to the total radius r_{tot} is given for the individual components. k_{hc} and f_{hc} for the heating cable core, k_h and f_h

for the heating cable protection, k_j and f_j for the DTS cable jacket, k_a and f_a for the DTS cable aramid protection, k_m and f_m for the DTS fibre mantle, k_f and f_f for the DTS fibre, f_{sed} and k_{eff} for the saturated sediment.

The parameter h is the heat transfer coefficient ($\text{W m}^{-2} \text{K}^{-1}$) defined by [6]:

$$h = \frac{k_{eff}}{L} Nu \quad (8)$$

where L is the characteristic length of the flow (m), Nu the Nusselt number. The combined thermal conductivity (k_{eff}) of sediment and water as given by [18]:

$$k_{eff} = nk_f + (1 - n)k_s \quad (9)$$

where n is the porosity and k_f and k_s the thermal conductivity of the water and the sediment solid material.

The Nusselt number showing the ratio of convective heat transport to conductive heat transport. It is related to the groundwater flow velocity (through the Reynolds number) and other conduction properties (through the Prandtl number). Empirical correlations between the Nusselt, Reynolds and Prandtl numbers exist for different flow conditions [26]. The authors of [27] identified an empirical relationship for external flow alongside a cylinder for low Reynolds numbers (laminar flow) in the form of:

$$Nu = C Re^m Pr^{\frac{1}{3}} \quad (10)$$

where Nu is the Nusselt number, Re is the Reynolds number, Pr is de Prandtl number and C and m are constants which are determined empirically based on the laboratory measurements. Standard values for C and m are available depending on the values for Re and Pr [26,27]. The Reynolds number and Prandtl number are defined as:

$$Re = \frac{\rho u L}{\mu} = \frac{u L}{\nu} \quad (11)$$

$$Pr = \frac{C_f \mu}{k_f} \quad (12)$$

where ρ is the density of the water (in kg m^{-3}), u is the flow velocity (in m s^{-1}), μ is the dynamic viscosity of the water ($\text{kg m}^{-1} \text{s}^{-1}$), and ν is the kinematic viscosity of the water (in $\text{m}^2 \text{s}^{-1}$), C_f is the specific heat capacity of the fluid (in $\text{J kg}^{-1} \text{°C}^{-1}$). For L we used the diameter of the heating cable.

Using the experimental data to determine values for C and m for our setup, based on Equation (6), an equation for the groundwater flow velocity with measured ΔT as input can be written as [15]:

$$u = \left(\frac{p}{\frac{\Delta T 2\pi}{Q} + \left(\frac{1}{k_{tot}} \ln\left(\frac{r_{tot}}{r_{h1}}\right) \right)} \right)^{1/m} \quad (13)$$

with p a constant defined by:

$$p = \frac{L \nu^m}{r_{h2} k_{eff} C Pr^{1/3} L^m} \quad (14)$$

The promise is that using the experimentally determined values of C and m and assuming these to be applicable for the current cable setup, Equations (7), (9) and (12)–(14) can be used to determine groundwater flow velocities from observations of ΔT , from a similarly configured cable under field conditions as authors intend to test. The influence of the cable presence on the groundwater flow is incorporated in the FlexPDE modeling but is not specifically considered in Equation (13). The constants C and m are however fitted based on the laboratory data results, including this effect in the fit. Appendix A presents the derivation of Equation (13) based on Equation (6).

3. Results

Results of the laboratory experiments are presented and used for calibration and validation of a numerical model of coupled heat transfer and fluid flow, and the analytical solution for the temperature difference and groundwater flow velocity relation, as derived above.

3.1. Experimental Results

In Figure 4, ΔT is plotted against the corresponding groundwater flow velocity for each experimental run and each location in the flow simulator for the experiments of July–August 2018 (cable setup as shown in Figure 3b). The data is plotted using box-whisker plots combining the results of all locations in the flow simulator for the specific measured groundwater flow velocity. These plots illustrate the decrease of ΔT with increasing groundwater flow velocity. An increase in groundwater flow velocity of 1 m d^{-1} results in a $0.38 \text{ }^\circ\text{C}$ lower ΔT for all data points. However, as suggested by Equation (13), the ΔT versus groundwater flow velocity relationship is non-linear, which was also concluded in a study using higher flow rates [8].

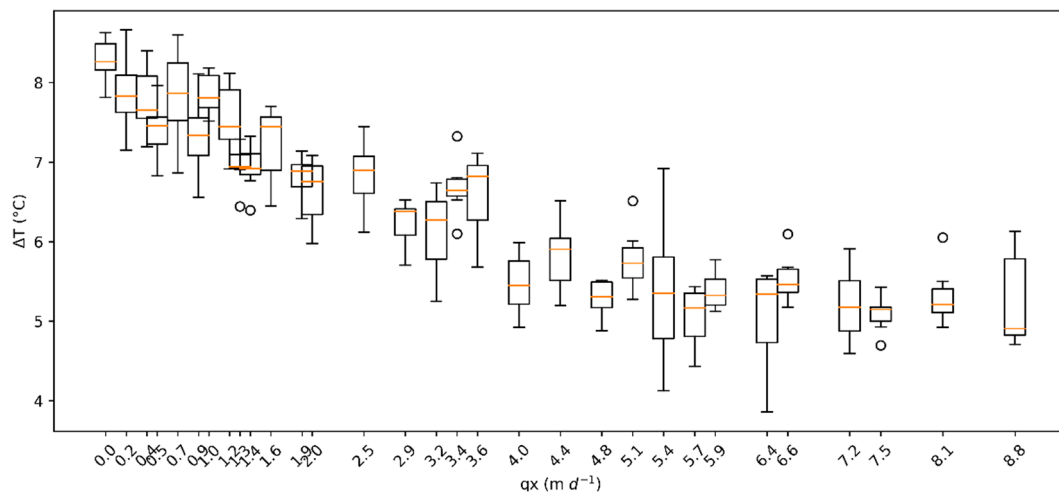


Figure 4. Box-whisker plots of the measured data from the flow simulator showing the groundwater flow velocity (x -axes) versus ΔT (Y -axes) for the data measured in the 2018 experiments. The measurement data for all measurement values of all cables in the experiments for a specific experimental run are combined into one box. The orange line of the box shows the median of the data, and the bottom and top edges of the box respectively the 25th and 75th percentiles. The whiskers stretch to the most extreme datapoints not being outliers that are marked as open circle markers.

3.2. Analyzing Results with a Numerical Modeling Code (FlexPDE)

The observations from the laboratory experiments were subsequently used for optimization and calibration of the FlexPDE model described in Section 2.3. The temperature development over time during heating by the heating wires was modeled for the same duration and flow settings as during the experimental runs (Figure 5). The temperature calculated in the model at the center of the modeled fiber-optic cables was compared to the measurement data of the DTS cable for location A4 (Figure 6) and A3 (Figure 7).

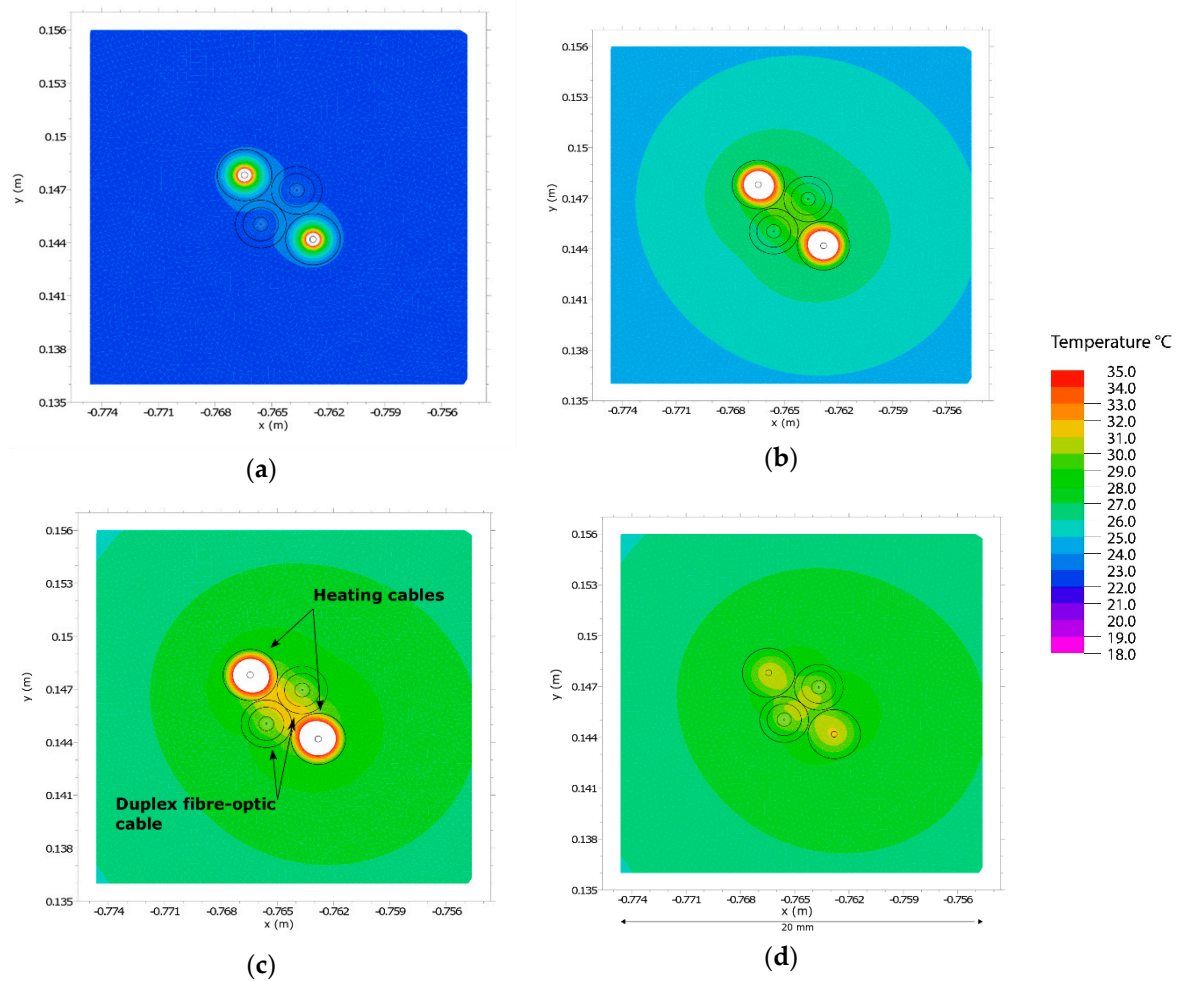


Figure 5. Temperature of the groundwater as modeled in FlexPDE. The direct surroundings of the Active Heating-Distributed Temperature Sensing (AH-DTS) cable at location A3 is shown, containing the duplex fiber-optic cable and the two heating cables. The flow is from left to right. Plotted area $20\text{ mm} \times 20\text{ mm}$ of the $2\text{ m} \times 1\text{ m}$ modeled area; (a) temperature in and around the cable at time 2200 s; (b) at time 2790 s; (c) at time 9390 s; (d) at time 9400 s.

The comparison of the measured temperature by the fiber-optic cable and the temperature modeled at location A3 was used to determine the thermal conductivity of the solid particles (k_s) of the sediment. In the first calibration round the thermal conductivity was varied between 4 and $7\text{ W m}^{-1}\text{ K}^{-1}$ in steps of $0.5\text{ W m}^{-1}\text{ K}^{-1}$. Table 3 shows the mean absolute errors for the calibration location A4 and the validation location A3.

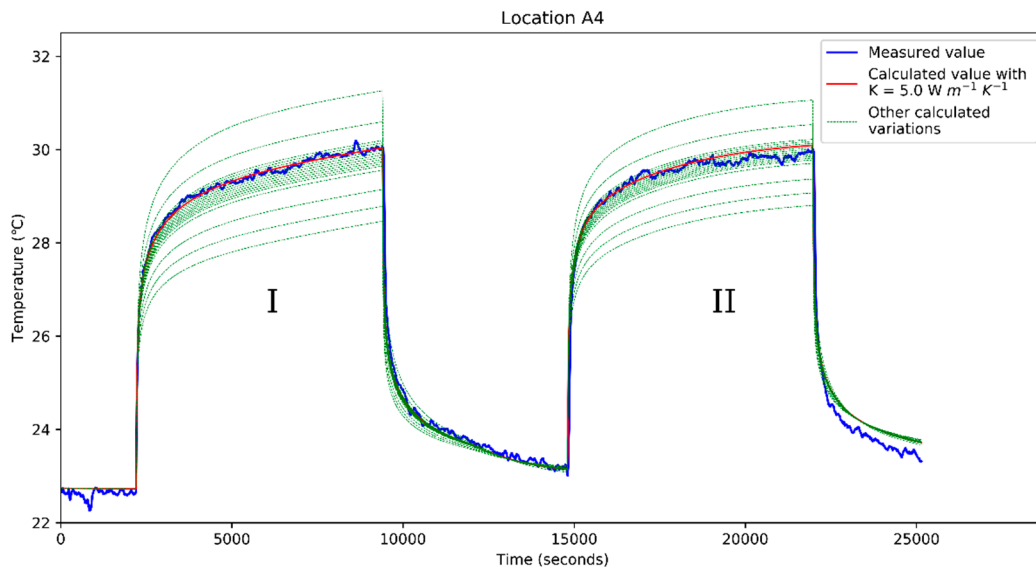


Figure 6. Comparison of model and measurement data for the calibration location A4 in the flow simulator for three experimental runs. The blue line shows the temperature as measured in the experiments, the red line the modeled temperature for the best fit solution. The dotted green lines present the variations of K_s that were calculated.

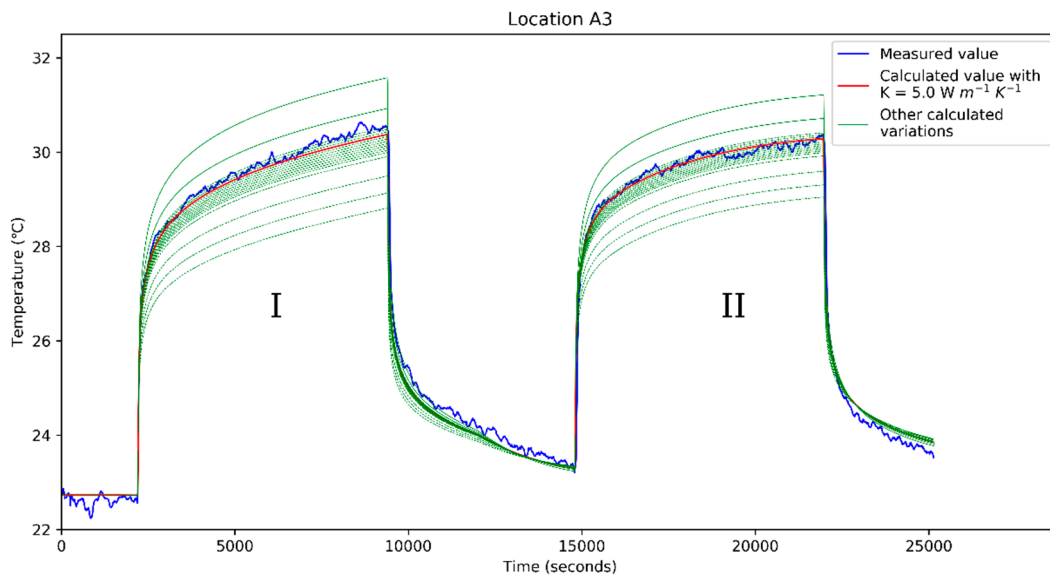


Figure 7. Comparison of model and measurement data for the validation location A3 in the flow simulator for three experimental runs. The blue line shows the temperature as measured in the experiments, the red line the modeled temperature for the best fit solution. The dotted green lines present the variations of K_s that were calculated.

Based on the results of the first calibration round, a second round of simulation with steps of $0.05 \text{ W m}^{-1} \text{ K}^{-1}$ was used to determine the best fit solution by minimizing the error. The mean absolute errors for the variations of the second calibration round are provided in Table 4. A best fit between observations and model data was obtained for $K_s = 5.0 \text{ W m}^{-1} \text{ K}^{-1}$, within ranges ($2\text{--}8.4 \text{ W m}^{-1} \text{ K}^{-1}$) found in literature [19,28,29].

Table 3. Mean absolute error between model estimation and measurement results of the first calibration round.

Thermal Conductivity (W m ⁻¹ K ⁻¹)	Location A4 (°C)	Location A3 (°C)
4.0	0.670	0.596
4.5	0.372	0.323
5.0	0.149	0.172
5.5	0.322	0.382
6	0.523	0.581
6.5	0.700	0.758
7	0.857	0.914

Table 4. Mean absolute error between model estimation and measurement results for the second calibration round.

Thermal Conductivity (W m ⁻¹ K ⁻¹)	Location A4 (°C)	Location A3 (°C)
4.85	0.192	0.164
4.9	0.172	0.159
4.95	0.156	0.162
5.0	0.149	0.172
5.05	0.152	0.188
5.1	0.163	0.207
5.15	0.178	0.227
5.2	0.195	0.249
5.25	0.215	0.271
5.3	0.236	0.294
5.35	0.257	0.316
5.4	0.279	0.338

The calculated and measured temperature for calibration location A4 is shown in Figure 6. In the first heating run (I) the modeled value matches correctly with the measurement data. For the second heating run (II) a slight overestimating can be seen also resulting in an overestimation of the base temperature after the heating run.

The model was validated by checking its predictive capacity at a different location A3 (Figure 7). For the first heating run (I) the model slightly underestimates the measured temperature. The second heating run (II) is a correct fit with the measured temperature. As Tables 3 and 4 show, the chosen model is also the best fit for the validation location.

3.3. Applying Analytical Solution (Equation (13)) for Flow Velocity Estimation

By solving Equation (13) using the experimental data, the constants C and m are estimated a priori. Due to the different cable setups for the experiments in 2017 and 2018, also the C and m constants differ for the 2017 and 2018 datasets. For the optimal cable, as used in the experiments of 2018, C and m are respectively estimated as 0.471 and 0.217.

Using the estimated constants C and m , Equation (13) is applied to estimate the groundwater flow velocity based on the measured ΔT . The result is plotted together with the experimental results (mean values per groundwater flow velocity) for the 2018 data (Figure 8). The fraction explained variance $R^2 = 0.85$. ΔT ranged from 5 to 8.4 °C with flow velocities up to 8.8 m d⁻¹. The calculated velocities are in line with the measured velocities.

The modeled groundwater flow velocity using Equation (13) results in a good fit to the measurement data for low ΔT ($\Delta T < 7$ °C) and accordingly higher flow velocities (Figure 8). For higher ΔT , the flow velocity is overestimated by the equation compared to the measurement data.

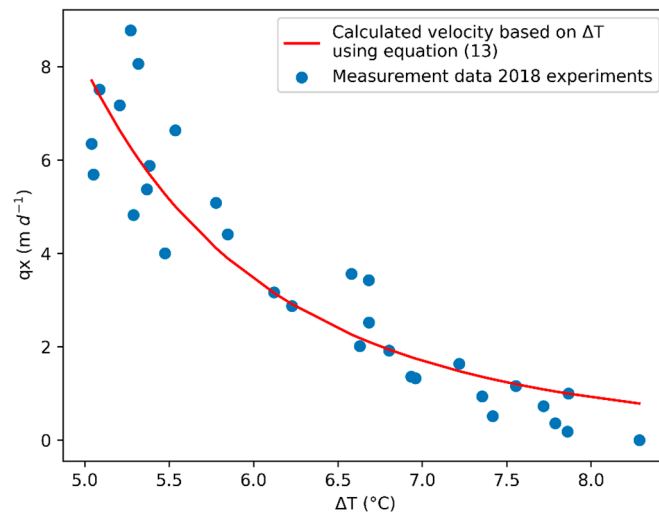


Figure 8. Measured ΔT groundwater flow velocity and the modeled groundwater flow velocity (Equation (13)) using measured ΔT as input shown for the 2018 experiments for the optimized C and m constants.

4. Discussion

Higher groundwater flow velocities were measured during the experiments for similar ΔT values compared to the model prediction using Equation (13). This difference can be partly explained by the challenge of realizing low groundwater flow velocities in the flow simulator. Groundwater flow velocities in the flow simulator below 0.5 m d^{-1} were relatively unstable. The hydraulic head difference between the in- and outflow of the flow simulator for these flow velocities needed to be very low ($<2.5 \text{ cm}$) which is difficult to control with the relative coarse sand used in the experiment. Small fluctuations in the in- and outflow system can have a significant effect.

The 2017 experiments (see description in Section 2.2) provided useful insights for realizing the successful 2018 results. The 2017 experiments showed the importance of a controlled background temperature in the flow simulator. Changes in the inflow temperature resulted in the need for a correction of the shift in the background temperature. In the 2018 experiments, we were able to maintain a more stable background temperature, without irregular temperature changes, by keeping the flow running overnight. The improvements to the cable setup, the use of two heating wires directly connected to the fiber-optic cable, made the results from the 2018 dataset more reliable. The distance between the heating wire and fiber-optic cable in the numerical modeling efforts and solving Equations (6) and (13), was now known and constant. The heating cycles were increased up to 90–120 min duration in the 2018 experiments (2017: 30–45 min) resulting in more reliable fits for the equilibrium temperatures.

Although Equation (13) proves useful for estimating the groundwater flow velocity based on ΔT in our results, we stress that the values of the empirical constants C and m are dependent on the flow geometry around the cable and thus on the cable setup. As a result, C and m must be defined based on controlled experiments similar to our study for each specific cable setup before the cable setup in combination with Equation (13) can be used in field studies. C and m are related to Reynolds and Prandtl numbers, both being a function of the fluid motion [6]. As a next step, the analytical solution could be further analyzed using numerical modeling, giving insight on the sensitivity of the empirical constants and their physical meaning.

Our analyses focused on the ΔT –groundwater flow velocity relation based on the maximum temperature increase observed at the heating cable during heating. We consider that the heating curve itself may hold a clearer relationship with the groundwater flow velocity being less dependent on variation in background temperature. An alternative approach is to derive an analytical equation

predicting the entire increase of temperature over time during heating, e.g., such as the well function proposed by [7]. By solving the model for $t \rightarrow \infty$ and inverting this formula to calculate the groundwater flow velocity a similar result can be reached. However, to fit such an equation to our cable setup, this equation needs to be extended to include the material properties of the heating cable. Furthermore, similar to our approach, parameters need to be fitted on a known dataset for the specific cable setup at hand for field applications.

5. Conclusions

We measured the maximum temperature difference (ΔT) using an AH-DTS fiber-optic cable setup placed inside a groundwater flow simulator, controlling and measuring the groundwater flow velocities. An equation was developed to calculate groundwater flow velocity by measured ΔT resulting from heating the AH-DTS cable for a fixed period and constant power. The ΔT was extracted from the data by estimating the equilibrium temperature of curves fitted to the measured heating and cooling curves of the data. We derived an analytical solution based on the heat equation that can be used to explicitly calculate groundwater flow velocity from measured ΔT for this specific AH-DTS setup. The constants C and m of this equation have to be determined a priori in the lab and are specific for the cable setup used. The calculated groundwater flow velocities are consistent with the measurement data, making the equation useful for field applications of this specific AH-DTS cable setup.

Note that this specific AH-DTS setup tested in our laboratory experiment will in the future be applied at a field site, near a drinking water extraction well in the east of the Netherlands. The resulting analytical solution will thus be used to estimate groundwater flow velocity based on the measured temperature difference (ΔT) at this field site.

Author Contributions: Conceptualization, W.B., V.B., G.O. and M.B.; methodology, W.B., R.W. and V.B.; software, W.B. and R.W.; validation, W.B. and R.W.; formal analysis, W.B. and R.W.; investigation, W.B., P.D. and R.W.; resources, W.B. and P.D.; data curation, W.B. and P.D.; writing—Original draft preparation, W.B. and P.D.; writing—Review and editing, W.B., V.B., G.O. and M.B.; visualization, W.B. and R.W.; supervision, V.B., G.O. and M.B.

Funding: This work was performed in the cooperation framework of Wetsus, European Centre of Excellence for Sustainable Water Technology (www.wetsus.eu). Wetsus is cofunded by the Dutch Ministry of Economic Affairs and Ministry of Infrastructure and Environment, the European Union Regional Development Fund, the Province of Fryslân, and the Northern Netherlands Provinces.

Acknowledgments: The authors like to thank the participants of the research theme ‘Groundwater Technology’ for the fruitful discussions and their financial support.

Conflicts of Interest: The authors declare no conflict of interest.

Appendix A. Equation (13) Derived Based on Equation (6)

We present an equation for calculating the flow velocity based on the temperature difference measured (Equation (13) in article). This formula is based upon the formula presented by [6]. In this appendix we show how our equation is derived from the formula presented by [6]. A list of mentioned parameters is presented at the end of the appendix.

The equation presented (Equation (13) in article):

$$u = \left(\frac{p}{\frac{\Delta T 2\pi}{Q} + \left(\frac{1}{k_{tot}} \ln \left(\frac{r_{tot}}{r_{h1}} \right) \right)} \right)^{1/m} \quad (A1)$$

With p a constant defined by (Equation (14) in article)

$$p = \frac{L v^m}{r_{h2} K_{eff} C Pr^{1/3} L^m} \quad (A2)$$

This equation is based upon the equation presented by [6]:

$$\Delta T = \frac{Q}{2\pi} \left(\frac{1}{h r_{h2}} + \frac{1}{k_{tot}} \ln \frac{r_{tot}}{r_{h1}} \right) \tag{A3}$$

Equation (A1) can be derived based on Equation (A3) by rewriting Equation (A3) as

$$\frac{\Delta T 2\pi}{Q} = \frac{1}{h \Delta r_{h2}} + \frac{1}{k_{tot}} \ln \frac{r_{tot}}{r_{h1}} \tag{A4}$$

Then excluding h

$$h = \frac{1}{r_{h2} \left(\frac{\Delta T 2\pi}{Q} - \frac{1}{k_{tot}} \ln \frac{r_{tot}}{r_{h1}} \right)} \tag{A5}$$

With h is defined by the Nusselt number which is defined by the Reynolds number and the Prandtl number and can be written as,

$$h = \frac{k_{eff}}{L} C \left(\frac{uL}{\nu} \right)^m Pr^{\frac{1}{3}} \tag{A6}$$

Resulting in

$$\frac{k_{eff}}{L} C \left(\frac{uL}{\nu} \right)^m Pr^{\frac{1}{3}} = \frac{1}{r_{h2} \left(\frac{\Delta T 2\pi}{Q} - \frac{1}{k_{tot}} \ln \frac{r_{tot}}{r_{h1}} \right)} \tag{A7}$$

Equation (A7) can be rewritten to

$$\frac{L}{r_{h2} \left(\frac{\Delta T 2\pi}{Q} - \frac{1}{k_{tot}} \ln \frac{r_{tot}}{r_{h1}} \right) k_{eff} C Pr^{\frac{1}{3}}} = \left(\frac{uL}{\nu} \right)^m \tag{A8}$$

Equation (A8) can be rewritten to

$$\frac{L}{r_{h2} \left(\frac{\Delta T 2\pi}{Q} - \frac{1}{k_{tot}} \ln \frac{r_{tot}}{r_{h1}} \right) k_{eff} C Pr^{\frac{1}{3}}} = \frac{u^m L^m}{\nu^m} \tag{A9}$$

The velocity can be separated from Equation (A9)

$$\frac{L \nu^m}{r_{h2} \left(\frac{\Delta T 2\pi}{Q} - \frac{1}{k_{tot}} \ln \frac{r_{tot}}{r_{h1}} \right) k_{eff} C Pr^{\frac{1}{3}} L^m} = u^m \tag{A10}$$

And

$$u = \left(\frac{L \nu^m}{r_{h2} \left(\frac{\Delta T 2\pi}{Q} - \frac{1}{k_{tot}} \ln \frac{r_{tot}}{r_{h1}} \right) k_{eff} C Pr^{\frac{1}{3}} L^m} \right)^{1/m} \tag{A11}$$

By defining constant p (Equation (A2)), Equation (A11) can be simplified to Equation (A1).

Parameters:

- Q as heat input to the cable ($W m^{-1}$),
- r_{h1} the radius of the heating part of the heating cable (m),
- r_{h2} the total radius of the heating cable (m),
- r_{tot} is the sum of the radii of the heating cable, the distance through the sediment and the radius of the fiber-optic cable used to measure temperature change combined (m),
- ΔT as the temperature change due to heating ($^{\circ}C$), and
- k_{tot} is the combined thermal conductivity calculated (harmonic mean) as materials in series [26]:

$$k_{tot} = \frac{1}{\frac{f_{hc}}{k_{hc}} + \frac{f_h}{k_h} + \frac{f_j}{k_j} + \frac{f_a}{k_a} + \frac{f_m}{k_m} + \frac{f_f}{k_f} + \frac{f_{sed}}{k_{eff}}} \quad (A12)$$

where the thermal conductivity (see Table 2) and the fraction of the thickness in respect to the total radius is given for the individual components. k_{hc} and f_{hc} for the heating cable core, k_h and f_h for the heating cable protection, k_j and f_j for the DTS cable jacket, k_a and f_a for the DTS cable aramid protection, k_m and f_m for the DTS fibre mantle, k_f and f_f for the DTS fibre, f_{sed} and k_{eff} for the saturated sediment.

- k_{hc} and f_{hc} are the thermal conductivity and fraction of thickness in respect to the total radius r_{tot} of the heating cable core,
- k_h and f_h are the thermal conductivity and fraction of thickness in respect to the total radius r_{tot} of the heating cable protection,
- k_j and f_j are the thermal conductivity and fraction of thickness in respect to the total radius r_{tot} of the DTS cable jacket,
- k_a and f_a are the thermal conductivity and fraction of thickness in respect to the total radius r_{tot} of the DTS cable aramid protection,
- k_m and f_m are the thermal conductivity and fraction of thickness in respect to the total radius r_{tot} of the DTS fiber mantle,
- k_f and f_f are the thermal conductivity and fraction of thickness in respect to the total radius r_{tot} of the DTS fiber,
- k_{eff} and f_{sed} are the thermal conductivity and fraction of thickness in respect to the total radius r_{tot} of the saturated sediment.
- Parameter h is the heat transfer coefficient ($\text{W m}^{-2} \text{K}^{-1}$) defined by [6]:

$$h = \frac{k_{eff}}{L} Nu \quad (A13)$$

- L is the characteristic length of the flow (m),
- Nu the Nusselt number (-),
- k_{eff} the combined thermal conductivity of sediment and water as given by [18]:

$$k_{eff} = nk_f + (1 - n)k_s \quad (A14)$$

- n is the porosity
- k_f and k_s the thermal conductivity of the water and the sediment solid material.
- The Nusselt number is given by

$$Nu = C Re^m Pr^{\frac{1}{3}} \quad (A15)$$

- Re is the Reynolds number (-)

$$Re = \frac{\rho u L}{\mu} = \frac{u L}{\nu}$$

- ρ the density of the water (in kg m^{-3})
- u the groundwater flow velocity (in m s^{-1})
- μ the dynamic viscosity of the water ($\text{kg m}^{-1} \text{s}^{-1}$)
- ν the kinematic viscosity of the water (in $\text{m}^2 \text{s}^{-1}$)

- Pr is de Prandtl number (-)

$$Pr = \frac{c_f \mu}{k_f}$$

- C_f the specific heat capacity of the fluid (in $\text{J kg}^{-1} \text{ }^\circ\text{C}^{-1}$)
- k_f is the thermal conductivity of the fluid (in $\text{W m}^{-1} \text{ }^\circ\text{C}^{-1}$)
- C and m are constants which are determined empirically and standard values for C and m are available depending on the values for Re and Pr (Hilpert, 1933; Bergman et al., 2011).

References

1. Burnett, B.; Chanton, J.; Christoff, J.; Kontar, E.; Krupa, S.; Lambert, M.; Moore, W.; O'Rourke, D.; Paulsen, R.; Smith, C.; et al. Assessing methodologies for measuring groundwater discharge to the ocean. *Eos Trans. Am. Geophys. Union (Wash. DC)* **2002**, *83*, 117–123. [[CrossRef](#)]
2. Sommer, W.; Valstar, J.; Leusbrock, I.; Grotenhuis, T.; Rijnaarts, H. Optimization and spatial pattern of large-scale aquifer thermal energy storage. *Appl. Energy* **2015**, *137*, 322–337. [[CrossRef](#)]
3. Greswell, R. *High-Resolution in Situ Monitoring of Flow between Aquifers and Surface Waters*; Environment Agency: Rio House, Waterside Drive, Aztec West, Almondsbury Bristol, UK, 2005.
4. Brouyère, S.; Batlle-Aguilar, J.; Goderniaux, P.; Dassargues, A. A new tracer technique for monitoring groundwater fluxes: The Finite Volume Point Dilution Method. *J. Contam. Hydrol.* **2008**, *95*, 121–140. [[CrossRef](#)] [[PubMed](#)]
5. Drost, W.; Klotz, D.; Koch, A.; Moser, H.; Neumaier, F.; Rauert, W. Point dilution methods of investigating ground water flow by means of radioisotopes. *Water Resour. Res.* **1968**, *4*, 125–146. [[CrossRef](#)]
6. Read, T.; Bour, O.; Selker, J.S.; Bense, V.; Le Borgne, T.; Hochreutener, R.; Lavenant, N. Active-distributed temperature sensing to continuously quantify vertical flow in boreholes. *Water Resour. Res.* **2014**, *50*, 3706–3713. [[CrossRef](#)]
7. Bakker, M.; Caljé, R.; Schaars, F.; Van Der Made, K.-J.; De Haas, S. An active heat tracer experiment to determine groundwater velocities using fiber optic cables installed with direct push equipment. *Water Resour. Res.* **2015**, *51*, 2760–2772. [[CrossRef](#)]
8. Aufleger, M.; Conrad, M.; Goltz, M.; Perzmaier, S.; Porras, P. Innovative dam monitoring tools based on distributed temperature measurement. *Jordan J. Civ. Eng.* **2007**, *1*, 29–37.
9. Bense, V.; Read, T.; Bour, O.; Le Borgne, T.; Coleman, T.; Krause, S.; Chalari, A.; Mondanos, M.; Ciocca, F.; Selker, J.S. Distributed Temperature Sensing as a downhole tool in hydrogeology. *Water Resour. Res.* **2016**, *52*, 9259–9273. [[CrossRef](#)]
10. Pehme, P.; Parker, B.; Cherry, J.; Greenhouse, J. Improved Resolution of Ambient Flow through Fractured Rock with Temperature Logs. *Ground Water* **2010**, *48*, 191–205. [[CrossRef](#)] [[PubMed](#)]
11. Banks, E.W.; Shanafield, M.A.; Cook, P.G. Induced Temperature Gradients to Examine Groundwater Flowpaths in Open Boreholes. *Ground Water* **2014**, *52*, 943–951. [[CrossRef](#)] [[PubMed](#)]
12. Read, T.; Bour, O.; Bense, V.; Le Borgne, T.; Goderniaux, P.; Klepikova, M.; Hochreutener, R.; Lavenant, N.; Boschero, V. Characterizing groundwater flow and heat transport in fractured rock using fiber-optic distributed temperature sensing. *Geophys. Res. Lett.* **2013**, *40*, 2055–2059. [[CrossRef](#)]
13. Selker, F.; Selker, J.S. Investigating Water Movement Within and Near Wells Using Active Point Heating and Fiber Optic Distributed Temperature Sensing. *Sensors* **2018**, *18*, 1023. [[CrossRef](#)] [[PubMed](#)]
14. Tombe, B.F.D.; Bakker, M.; Smits, F.; Schaars, F.; Made, K.; Van Der Made, K.-J.; Tombe, B.F.D. Estimation of the Variation in Specific Discharge Over Large Depth Using Distributed Temperature Sensing (DTS) Measurements of the Heat Pulse Response. *Water Resour. Res.* **2019**, *55*, 811–826. [[CrossRef](#)]
15. Van Weesep, R. Modelling Groundwater Flow Velocity Using Temperature Change Data from Active Distributed Temperature Sensing Measurements in Laboratory Experiments. Master's Thesis, University of Utrecht, Utrecht, The Netherlands, 2017.
16. Hausner, M.B.; Suarez, F.; Glander, K.E.; Van De Giesen, N.; Selker, J.S.; Tyler, S.W. Calibrating Single-Ended Fiber-Optic Raman Spectra Distributed Temperature Sensing Data. *Sensors* **2011**, *11*, 10859–10879. [[CrossRef](#)] [[PubMed](#)]

17. LEONI. Available online: www.leoni-fiber-optics.com (accessed on 15 May 2019).
18. Anderson, M.P. Heat as a Ground Water Tracer. *Groundwater* **2005**, *43*, 951–968. [[CrossRef](#)] [[PubMed](#)]
19. Farouki, O.T. *Thermal Properties of Soils*; U.S. Army Cold Regions Research and Engineering Laboratory: Hanover, NH, USA, 1981.
20. Hamdhan, I.N.; Clarke, B. Determination of thermal conductivity of coarse and fine sand soils. In Proceedings of the World Geotherm, Bali, Indonesia, 25–29 April 2010; pp. 1–7.
21. Abu-Hamdeh, N.H. Thermal Properties of Soils as affected by Density and Water Content. *Biosyst. Eng.* **2003**, *86*, 97–102. [[CrossRef](#)]
22. Sim, L.; Ramanan, S.; Ismail, H.; Seetharamu, K.; Goh, T. Thermal characterization of Al₂O₃ and ZnO reinforced silicone rubber as thermal pads for heat dissipation purposes. *Thermochim. Acta* **2005**, *430*, 155–165. [[CrossRef](#)]
23. Tomlins, P.E.; Rides, M.; Dawson, A.; Gee, M.; Dean, G.; Hobbs, C.; Allen, C.; Gnaniah, S.; Calver, A.; Darling, R. *Physical Characterisation of Soft-Touch Polymers*; National Physical Laboratory: Teddington, UK, 2005.
24. Dupont. *Kevlar Aramid Fiber Technical Guide*; Dupont: Richmond, VA, USA, 2017. Available online: www.dupont.com (accessed on 14 February 2019).
25. André, P.; Rocha, A.; Domingues, F.; Facão, M. Thermal Effects in Optical Fibres. In *Developments in Heat Transfer*; InTech: Haverhill, MA, USA, 2011; Volume 1987. Available online: <http://www.intechopen.com/books/developments-in-heat-transfer/thermal-effects-in-optical-fibres> (accessed on 4 August 2019).
26. Bergman, T.L.; Incropera, F.P.; Lavine, A.S.; DeWitt, D.P. *Fundamentals of Heat and Mass Transfer*; John Wiley & Sons: Hoboken, NJ, USA, 2011; ISBN 978-0470501979.
27. Hilpert, R. Wärmeabgabe von geheizten Drähten und Rohren im Luftstrom. *Forsch. Ing.* **1933**, *4*, 215–224. [[CrossRef](#)]
28. Powell, R.W.; Ho, C.Y.; Liley, P.E. *Thermal Conductivity of Selected Materials*; U.S. Department of Commerce: Washington, DC, USA, 1966.
29. Tarnawski, V.R.; Momose, T.; Leong, W.H. Thermal Conductivity of Standard Sands II. Saturated Conditions. *Int. J. Thermophys.* **2011**, *32*, 984–1005. [[CrossRef](#)]



© 2019 by the authors. Licensee MDPI, Basel, Switzerland. This article is an open access article distributed under the terms and conditions of the Creative Commons Attribution (CC BY) license (<http://creativecommons.org/licenses/by/4.0/>).